Flatfielding in spatial heterodyne spectroscopy

Christoph R. Englert and John M. Harlander

Spatial heterodyne spectroscopy (SHS) is a Fourier-transform spectroscopic technique that simultaneously records all path differences using a detector array. Compared to conventional Fourier-transform spectroscopy that measures interferogram samples sequentially in the time domain, SHS is insensitive to a changing scene; however, the effects caused by differences in the detector elements and/or the optics for each sample must be addressed with a flatfield correction. The flatfield correction is typically a characteristic of the instrument and does not change with the observed scene. We present three different flatfielding approaches. Each is based on different assumptions and is applicable depending on the instrumental effects dominating the flatfield.

OCIS codes: 300.6300, 120.2650, 040.5160.

1. Introduction

Spatial heterodyne spectroscopy (SHS) is a technique that makes use of a spatially scanned interferometer. This class of interferometers is receiving increased attention in the experimental spectroscopy community.[1] The basic SHS configuration is similar to that of a Michelson interferometer used for Fourier-transform spectroscopy (FTS) with the return mirrors replaced by fixed diffraction gratings as shown in Fig. 1. The simplest explanation of the SHS principle is to consider the plane wavefronts entering the interferometer as indicated by the dashed line following L_1 in Fig. 1. At the exit of the interferometer the resulting two wavefronts are tilted with respect to each other with a wavenumber-dependent tilt angle. These crossed wavefronts produce a Fizeau fringe pattern that is imaged on the detector array. Zero spatial frequency corresponds to the Littrow wavenumber of the gratings. For other wavenumbers the spatial frequency is proportional to the difference between the signal wavenumber and the Littrow wavenumber. The fringe pattern recorded by the detector array is therefore equivalent to the Fourier transform of the incident spectrum that is heterodyned around the Littrow wavenumber. A defining characteristic of SHS instruments is that they achieve the theoretical resolution of the dispersive elements (gratings) but have the large throughput associated with interferometers (including the possibility of field widening) with no moving parts. A detailed description of the SHS concept can be found in publications by Harlander *et al.*[2–4]

One major difference between SHS and a conventional FTS is that a FTS interferogram is recorded in the time domain by a single detector, whereas the entire SHS interferogram is recorded simultaneously with multiple detector elements. As a consequence, the SHS interferogram is not compromised by temporal source variations, which contaminate the spectral information in the FTS case. On the other hand, every SHS interferogram sample is recorded using a different detector element, and the signal uses different paths through the interferometer optics for each interferogram sample (see Fig. 1). If the sample-to-sample variations are not deemed negligible, a flatfield correction must be applied. These intersample variations are similar to a temporally changing scene in the FTS case, with the important difference that in SHS the variations are a constant characteristic of the spectrometer and do not depend on the detected scene, thus making a scene-independent correction possible.

We adapt the term "flatfielding" for this correction since it is commonly used for the elimination of pixel-to-pixel variations in imaging detectors, which is a closely related problem. Here we present three SHS flatfielding approaches. The first one is suitable for instruments in which the detector pixel-to-pixel sensitivity variation dominates. The second one is suit-

C. R. Englert (Christoph.Englert@nrl.navy.mil) is with the Space Science Division, Code 7641, U.S. Naval Research Laboratory, 4555 Overlook Avenue, SW, Washington, D.C. 20375. J. M. Harlander is with the Department of Physics, Astronomy, and Engineering Science, St. Cloud State University, 720 Fourth Avenue South, MS-315, St. Cloud, Minnesota 56301.

Received 20 October 2005; revised 14 December 2005; accepted 27 December 2005; posted 4 January 2006 (Doc. ID 65451).

0003-6935/06/194583-08$15.00/0

Report Documentation Page

Form Approved
OMB No. 0704-0188

1. REPORT DATE	2. REPORT TYPE	3. DATES COVERED
14 DEC 2005		**00-00-2005 to 00-00-2005**

4. TITLE AND SUBTITLE	5a. CONTRACT NUMBER
Flatfielding in spatial heterodyne spectroscopy	5b. GRANT NUMBER
	5c. PROGRAM ELEMENT NUMBER
6. AUTHOR(S)	5d. PROJECT NUMBER
	5e. TASK NUMBER
	5f. WORK UNIT NUMBER
7. PERFORMING ORGANIZATION NAME(S) AND ADDRESS(ES) **Naval Research Laboratory,Space Science Division, Code 7641,4555 Overlook Avenue SW,Washington,DC,20375**	8. PERFORMING ORGANIZATION REPORT NUMBER
9. SPONSORING/MONITORING AGENCY NAME(S) AND ADDRESS(ES)	10. SPONSOR/MONITOR'S ACRONYM(S)
	11. SPONSOR/MONITOR'S REPORT NUMBER(S)

12. DISTRIBUTION/AVAILABILITY STATEMENT
Approved for public release; distribution unlimited

13. SUPPLEMENTARY NOTES

14. ABSTRACT

15. SUBJECT TERMS

16. SECURITY CLASSIFICATION OF:			17. LIMITATION OF ABSTRACT	18. NUMBER OF PAGES	19a. NAME OF RESPONSIBLE PERSON
a. REPORT	b. ABSTRACT	c. THIS PAGE			
unclassified	**unclassified**	**unclassified**	**Same as Report (SAR)**	**8**	

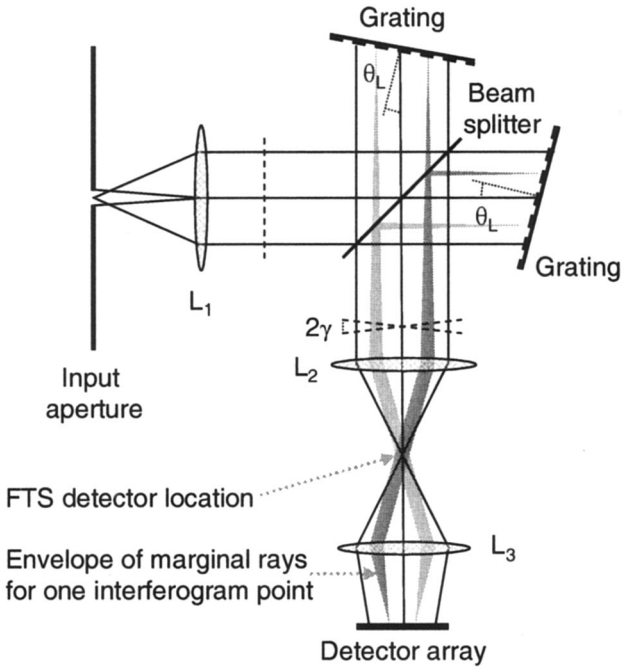

Fig. 1. Schematic diagram of basic non-field-widened SHS configuration. The dashed lines illustrate incoming wavefronts and the corresponding exiting wavefronts that are crossed with an angle of 2γ. The ray bundle for two interferogram samples is outlined showing that only a small section of the interferometer and optics is used for any individual interferogram sample.

able if, in addition to the detector sensitivity variations, the signal from both interferometer arms is not identical, e.g., due to the beam-splitter performance. The third approach is suitable for cases in which a spatial variability (e.g., scratches, manufacturing defects, or surface contamination) in the grating performance also plays a significant role.

Before we present the flatfielding techniques, we introduce the raw SHS interferogram, which is the fundamental equation for the discussion in Section 2.

2. Raw Spatial Heterodyne Spectroscopy Interferogram

Using the small-angle approximation, the ideal SHS interferogram can be written as[2]

$$I(x) = \frac{1}{2}\int_0^\infty B_\sigma(\sigma)[1 + \cos\{2\pi[4(\sigma - \sigma_0)\tan\theta_L]x\}]\mathrm{d}\sigma, \tag{1}$$

where $B_\sigma(\sigma)$ is the wavenumber-dependent spectral density, σ_0 is the Littrow wavenumber for which the recorded fringe frequency is zero, θ_L is the grating angle, and x is the pixel location. The leading factor of ½ accounts for the fact that, as in FTS, half of the incident signal leaves the interferometer through the input port, and half is detected at the output port. To simplify the following steps, we introduce the heterodyned fringe frequency $\kappa \equiv 4(\sigma - \sigma_0)\tan\theta_L$ and the heterodyned spectral density $B(\kappa) \equiv [B_\sigma(\sigma_0 + \kappa/4\tan\theta_L) + B_\sigma(\sigma_0 - \kappa/4\tan\theta_L)]/4\tan\theta_L$ with $\kappa > 0$. Using these definitions we get

$$I(x) = \frac{1}{2}\int_0^\infty B(\kappa)[1 + \cos\{2\pi\kappa x\}]\mathrm{d}\kappa, \tag{2}$$

showing that the heterodyned spectral density is essentially the Fourier transform of the modulated part of the interferogram. Note that the signals from the upper ($\sigma > \sigma_0$) and lower ($\sigma < \sigma_0$) sideband of the spectral density both result in positive fringe frequencies and therefore are superimposed in the spectrum retrieved by Fourier transformation of the interferogram unless one sideband is suppressed by a spectral prefilter. Harlander *et al.*[2] detailed a technique for unambiguously separating these sidebands by using a cross tilt in the grating alignment and employing a two-dimensional Fourier transform to generate the spectrum.

In practice, nonideal instrument properties can have additional effects on the raw interferogram. The raw interferogram measured along one row of a SHS detector array can generally be represented as

$$\begin{aligned} I(x) = \int_0^\infty B(\kappa)\{&t_A^2(x, \kappa) + t_B^2(x, \kappa) \\ &+ 2\varepsilon(x, \kappa)t_A(x, \kappa)t_B(x, \kappa) \\ &\times \cos[2\pi\kappa x + \Theta(x, \kappa)]\}\mathrm{d}\kappa, \end{aligned} \tag{3}$$

where $\varepsilon(x, \kappa)$ is the modulation efficiency, and $\Theta(x, \kappa)$ is a phase distortion term. The terms $t_A^2(x, \kappa)$ and $t_B^2(x, \kappa)$ are the intensity transmission functions for the signal passing through the two interferometer arms A and B, multiplied by the individual detector responsivity. The resulting raw interferogram $I(x)$ is generally recorded in digital units using an analog-to-digital converter (ADU). The raw measurement is subsequently calibrated yielding the spectral radiance of the source. The calibration generally requires proper flatfielding, therefore we will use raw interferograms in Section 5.

Equation (3) is a general representation of a SHS interferogram and allows for all possible spectral and spatial dependencies. For an ideal SHS instrument, $t_A^2(x, \kappa)$ and $t_B^2(x, \kappa)$ are identical (1/4) and do not depend on x or κ, $\Theta(x, \kappa)$ is zero, and $\varepsilon(x, \kappa)$ is close to unity for zero optical path difference and slowly decreases for higher path differences due to the finite étendue of the interferometer.[5]

It has been shown in the work of Harlander *et al.*[3] and Englert *et al.*[6] that a phase distortion can be corrected without impacting the envelope of the modulated part of the interferogram. Nevertheless, we will carry the phase distortion term along to show that it does not affect the flatfielding and that it is conserved by the flatfielding. We further make the assumption that the spectral dependence of $t_A^2(x, \kappa)$ and $t_B^2(x, \kappa)$ is identical for both arms so it can be separated into the function $R(\kappa)$, and we can write

$$I(x) = \int_0^\infty B(\kappa)R(\kappa)\{t_A{}^2(x) + t_B{}^2(x) + 2\varepsilon(x,\ \kappa)t_A(x)t_B(x)\cos[2\pi\kappa x + \Theta(x,\ \kappa)]\}\mathrm{d}\kappa, \tag{4a}$$

$$I(x) = \underbrace{\int_0^\infty B(\kappa)R(\kappa)[t_A{}^2(x) + t_B{}^2(x)]d\kappa}_{\text{Nonmodulated term}} + \underbrace{\int_0^\infty 2B(\kappa)R(\kappa)\varepsilon(x,\ \kappa)t_A(x)t_B(x)\cos[2\pi\kappa x + \Theta(x,\ \kappa)]\mathrm{d}\kappa}_{\text{Modulated term}} \tag{4b}$$

A consideration of the effects contributing to the spectral dependences of $t_A{}^2(x, \kappa)$ and $t_B{}^2(x, \kappa)$ confirms that this assumption is good: the spectral dependence due to the spectral response of the detector elements is by design identical for the signal of both arms. The design of both interferometer arms is identical so that the spectral dependence of the grating efficiency, the optical transmittance, reflectance, and scattering occurring on all optical elements in the instrument can safely be assumed to be identical for both arms. Furthermore, for SHS instruments that have a very narrow bandpass [e.g., 3 nm in the near UV for the Spatial Heterodyne Imager for Mesospheric Radicals (SHIMMER) on STPSat-1 (Space Test Program Satellite-1)[7]], spectral dependencies are not only very similar for both arms, but also very small. Note that this assumption does not imply a 50%/50% beam splitter, but only that the spectral dependence of the beam-splitter reflection and the transmission are equal for both arms.

3. Effects of Nonideal Flatfields

The goal of the SHS flatfield correction is to eliminate the interpixel variations introduced into the interferogram through the terms $t_A(x)$, $t_B(x)$, and $\varepsilon(x, \kappa)$.

The most straightforward nonideal flatfield is caused by a random pixel sensitivity variation across the detector, which results in a multiplicative function applied to the perfect interferogram and a decreased signal-to-noise ratio in the retrieved spectrum. If we assume an otherwise ideal double sided interferogram with N pixels and a random, relative pixel sensitivity variation of $\delta s/s$, the signal-to-noise ratio in the retrieved spectrum will be between $\sqrt{N/2}s/\delta s$ and $\sqrt{2/N}s/\delta s$, where the two extreme cases result from multiplex noise propagation assuming a single, unresolved line and a continuum spectrum, respectively. For $N = 640$ and a random pixel sensitivity variation of $\delta s/s = 5\%$, for example, the uncorrected flatfield would cause a signal-to-noise ratio in the spectrum of between 357.8 and 1.1, depending on the spectral content of the source. This simple example demonstrates that flatfield effects can have a serious impact on the quality of the retrieved spectra, especially for full spectra that do not contain only a few isolated emission lines.

In case the flatfield shows a significant structure, for example, a scratch in the grating or a significant decrease in modulation efficiency toward the edge of the detector, it is also appropriate to interpret the effect of the flatfield as a change in the instrumental line shape function. As shown in Eq. (4b), the uncorrected flatfield results in multiplicative functions for the nonmodulated and modulated part of the interferogram. The multiplicative functions are equivalent to convolution kernels in the spectral domain that have to be applied to the interferogram terms. The changed instrumental line shape typically results in a lower spectral resolution and in systematic errors from the incomplete removal of the contributions from the nonmodulated interferogram term. In general, flatfield errors result in higher noise, lower spectral resolution, and systematic errors in the retrieved spectrum.

The magnitude of the introduced errors obviously depends on the severity of the flatfield variations. In Subsection 5.D we present an example of a measured, flatfield corrected spectrum and the difference to the uncorrected spectrum by using a monochromatic source (see Fig. 6).

4. Flatfielding Techniques

We consider three flatfielding techniques in this paper, which should be applied depending on what instrumental effects dominate the variations in the flatfield. In Subsections 4.A–4.C we describe these three flatfielding approaches and the conditions under which their application is suitable. In Section 5 we illustrate the flatfielding problem using data taken with a breadboard SHS instrument.

A. Balanced Arm Flatfielding Approach

The balanced arm flatfielding approach is the simplest of the three. It is based on the assumption that $t_A(x) \equiv t_B(x)$, or that the signal from both interferometer arms is equal or balanced. This is a good assumption when the spatial variability of $t_A(x)$ and $t_B(x)$ is dominated by the sensitivity of the detector elements. In this case, the flatfield is independent of the interferometer arm (A or B) that the signal passes through. This approach does not correct for decreased fringe modulation due to an efficiency mismatch between the interferometer arms.

The idea behind this approach is to measure the nonmodulated part of the interferogram, which can be accomplished in a number of ways. One way is to

take two measurements, each with one interferometer arm blocked by inserting an opaque material between the beam splitter and the grating. The sum of the measurement with arm A blocked and the measurement with arm B blocked yields the nonmodulated part of the interferogram. Another method is to change the optical path in one of the arms during an exposure period by significantly more than one half of the longest observed wavelength, so that the modulation is completely washed out for all wavelengths. This can be done, for example, by pressure scanning one arm or tilting a plane-parallel plate in one arm.

The nonmodulated part of the interferogram can be written as

$$\begin{aligned} I_U(x) &= \int_0^\infty B_a(\kappa)R(\kappa)\left[t_A{}^2(x) + t_B{}^2(x)\right]\mathrm{d}\kappa \\ &= \left[t_A{}^2(x) + t_B{}^2(x)\right]\int_0^\infty B_a(\kappa)R(\kappa)\mathrm{d}\kappa \\ &= C_1\left[t_A{}^2(x) + t_B{}^2(x)\right], \end{aligned} \tag{5}$$

where C_1 is a scalar that depends on the spectrum of the observed source $B_a(\kappa)$. The ratio of the interferogram in Eq. (4b) and $I_U(x)$ yields

$$\begin{aligned} \frac{I(x)}{I_U(x)} = C_2 + \frac{1}{C_1}\int_0^\infty & B(\kappa)R(\kappa) \\ & \times \left\{ 2\varepsilon(x,\ \kappa)\ \frac{t_A(x)t_B(x)}{t_A{}^2(x) + t_B{}^2(x)} \right. \\ & \left. \times \cos[2\pi\kappa x + \Theta(x,\ \kappa)] \right\}\mathrm{d}\kappa, \end{aligned} \tag{6}$$

where the scalar C_2 is unity if the same source is used for both measurements. Using the above-mentioned assumption $t_A(x) \equiv t_B(x)$ we can write

$$\begin{aligned} \frac{I(x)}{I_U(x)} = C_2 + \frac{1}{C_1}\int_0^\infty & \{B(\kappa)R(\kappa)\varepsilon(x,\ \kappa) \\ & \times \cos[2\pi\kappa x + \Theta(x,\ \kappa)]\}\mathrm{d}\kappa. \end{aligned} \tag{7}$$

We have eliminated the interferogram sample (x) dependence in the nonmodulated term and only the scalar C_2 remains. After Fourier transformation into the spectral domain this scalar will contribute solely to the retrieved spectral density at the Littrow wavenumber (zero spatial frequency). Since all wavenumbers contribute a signal at zero spatial frequency through the nonmodulated term in Eq. (4b), most SHS instruments have eliminated any real spectral signal at zero spatial frequency by either choosing a spectral prefilter that is opaque at the Littrow wavenumber or by using a cross tilt in the grating alignment and employing a two-dimensional transform to generate the spectrum.[2] In these cases the additive term C_2 at zero spatial frequency can be ignored.

After phase distortion correction,[3,6] the second term of Eq. (5) is simply the cosine transform of the spectral intensity $B(\kappa)$ multiplied by $R(\kappa)/C_1$ and $\varepsilon(x, \kappa)$. $R(\kappa)/C_1$ represents the spectral response of the spectrometer. According to the convolution theorem, the modulation efficiency $\varepsilon(x, \kappa)$ represents the Fourier transform of the instrumental line shape function, which can be verified by measuring line sources.

B. Unbalanced Arm Flatfielding Approach

The unbalanced arm flatfielding approach does not require the balanced arm assumption $t_A(x) \equiv t_B(x)$, but requires instead the less stringent assumption that the integral in Eq. (6) is zero when averaged over all interferogram samples:

$$\left\langle \int_0^\infty B(\kappa)R(\kappa)\left\{ 2\varepsilon(x,\ \kappa)\ \frac{t_A(x)t_B(x)}{t_A{}^2(x) + t_B{}^2(x)} \times \cos[2\pi\kappa x + \Theta(x,\ \kappa)] \right\}\mathrm{d}\kappa \right\rangle_x = 0. \tag{8}$$

For slowly varying $t(x)$ and $\varepsilon(x, \kappa)$ and a negligible signal at low spatial frequencies this is a good assumption. This approach allows the correction of the interferogram if in addition to pixel-to-pixel sensitivity variations, the signal from both arms is not identical, e.g., because of the beam-splitter properties. Like the first approach, it also does not correct for modulation efficiency.

The idea behind this approach is to measure the nonmodulated part of the interferogram for the signal from each interferometer arm separately. By blocking interferometer arm B and A, one at a time, as described in Subsection 4.A we get the following two interferograms:

$$\begin{aligned} I_A(x) &= \int_0^\infty B_a(\kappa)R(\kappa)t_A{}^2(x)\mathrm{d}\kappa \\ &= t_A{}^2(x)\int_0^\infty B_a(\kappa)R(\kappa)\mathrm{d}\kappa = C_1 t_A{}^2(x), \end{aligned} \tag{9}$$

$$\begin{aligned} I_B(x) &= \int_0^\infty B_a(\kappa)R(\kappa)t_B{}^2(x)\mathrm{d}\kappa \\ &= t_B{}^2(x)\int_0^\infty B_a(\kappa)R(\kappa)\mathrm{d}\kappa = C_1 t_B{}^2(x). \end{aligned} \tag{10}$$

Again, C_1 is a scalar that depends on the spectrum of the observed source $B_a(\kappa)$. The ratio of the interferogram in Eq. (4b) and the sum of $I_A(x)$ and $I_B(x)$ yields

$$\frac{I(x)}{I_A(x)+I_B(x)} = C_2 + \underbrace{\frac{1}{C_1}\int_0^\infty B(\kappa)R(\kappa)2\varepsilon(x,\ \kappa)\frac{t_A(x)t_B(x)}{t_A^2(x)+t_B^2(x)}\cos[2\pi\kappa x+\Theta(x,\ \kappa)]\mathrm{d}\kappa}_{\text{Modulated term}}. \tag{11}$$

The next step is to subtract the scalar C_2. If the same source is used for the flatfield measurements $I_A(x)$ and $I_B(x)$ and the interferogram $I(x)$, then C_2 is unity and we can eliminate it by subtracting unity from Eq. (11). In the general case in which a different source is used for the interferogram $I(x)$, we can use the assumption of Eq. (8) and determine C_2 by calculating the average of the right-hand side of Eq. (11). After the subtraction of C_2 we can divide the modulated term in Eq. (11) by $\{2[I_A(x)I_B(x)]^{1/2}\}/[I_A(x) + I_B(x)]$ to get the flatfield corrected interferogram $I_C(x)$:

$$I_C(x) = \frac{1}{C_1}\int_0^\infty B(\kappa)R(\kappa)\varepsilon(x,\ \kappa)\cos[2\pi\kappa x+\Theta(x,\ \kappa)]\mathrm{d}\kappa. \tag{12}$$

This result is similar to the balanced-arm approach, but it properly corrects for the effect of unequal or unbalanced signal levels from the interferometer arms.

C. Phase-Shift Flatfielding Approach

The phase-shift flatfielding approach is motivated by measurements with spectrometers that show grating imperfections such as manufacturing defects, scratches, or surface dust particle contamination. These defects generally increase the scattering at the affected grating location and/or decrease the grating efficiency. The affected interferogram samples typically show lower overall signal levels and decreased modulation efficiency. These effects are generally wavelength independent, especially for narrowband instruments.

The goal of this flatfielding approach is to quantify the modulated and nonmodulated contribution to a monochromatic interferogram to provide a general flatfield correction that includes the effect of grating imperfections. This approach corrects for all flatfield effects, but it is also the most complex. It requires a monochromatic light source and the ability to change the optical path length in one interferometer arm.

The approach requires the measurement of three interferograms, each using the same monochromatic source, but different optical path lengths in one of the interferometer arms. The change in optical path length can be achieved by moving one grating, pressure scanning one arm, or tilting a plane-parallel plate in one arm. The resulting interferograms can be written as

$$\begin{aligned} I_i(x) &= B(\kappa_0)R(\kappa_0)\{t_A{}^2(x) + t_B{}^2(x) + 2\varepsilon(x,\ \kappa_0)t_A(x) \\ &\quad \times t_B(x)\cos[2\pi\kappa_0 x + \Theta(x,\ \kappa) + \varphi_i]\} \\ &= N(x,\ \kappa_0) + M(x,\ \kappa_0)\cos[2\pi\kappa_0 x + \Theta(x,\ \kappa) + \varphi_i], \\ &\quad i = 1,\ 2,\ 3\ \wedge\ \varphi_1 \neq \varphi_2 \neq \varphi_3. \end{aligned} \tag{13}$$

The next step is to determine the phases $\Phi_i(x) \equiv [2\pi\kappa_0 x + \theta(x, \kappa) + \varphi_i]$ for each measurement ($i = 1, 2, 3$) and each interferogram sample x. This can be achieved by using the technique described by Harlander *et al.*[3] and Englert *et al.*[6] It consists of Fourier transformation of the interferogram, isolation of the spectral line for positive frequencies, and backtransformation into the interferogram domain, where the ratio of the imaginary part and the real part is equivalent to the tangent of the phase. Note that this technique to determine the phase also accounts for phase distortions and slight changes in κ_0 that might result from a grating tilt during the translation of a grating. After determining the phases $\Phi_i(x)$, we can calculate the nonmodulated contribution $N(x, \kappa_0)$ and the amplitude of the modulated contribution $M(x, \kappa_0)$ of the interferograms for each interferogram sample using the above measurements:

$$M(x,\ \kappa_0) = \frac{I_i(x) - I_j(x)}{\cos\Phi_i(x) - \cos\Phi_j(x)}, \quad i \neq j, \tag{14}$$

$$N(x,\ \kappa_0) = I_1(x) - M(x,\ \kappa_0)\cos\Phi_1(x), \tag{15}$$

where i and j in Eq. (14) are chosen for each interferogram sample so that the denominator is never zero. This is the reason why three measurements with different phase offsets are necessary and two are not sufficient. It is best to choose i and j so that the absolute value of the denominator is as large as possible to avoid the division by a small number, which increases the uncertainty of the result when noise is present. A good choice for the three phase offsets $\varphi_{1/2/3}$ is, for example, 0°, 90°, and 180°, which causes the absolute value of the denominator in Eq. (14) to fall always between approximately 1 and $\sqrt{2}$.

We can now eliminate the nonmodulated contribution of any interferogram by dividing the interferogram by $N(x, \kappa_0)$ and subtracting the mean, similar to the unbalanced arm approach. Dividing the result by $M(x, \kappa_0)$ will remove the variations in modulation efficiency and the effects of the unbalanced arm signals' assumption of their wavelength independence.

Table 1. Key Design Parameters of the Visible/Near-Infrared SHS Breadboard Instrument

Parameter	Value/Description
Resolving power	~13 000
Bandpass	~700–900 nm
Beam splitter	Cubic, BK7
Gratings	60 grooves/mm, blazed
Exit optics	Telecentric lens, Magnification: 0.5
Spectral filter	Hoya R-72
Detector array	Micro-Pix M640 640 × 480, 7.4 μm pitch
Light source	Digikey M7805I 780 nm laser diode module

5. Flatfielding Examples Using Measured Data

A. Visible/Near-Infrared Breadboard Instrument

The data presented in the following subsections were measured with a visible/near-infrared breadboard SHS instrument.[8] The key instrument parameters and the light source used for the measurements are summarized in Table 1. Figure 2 shows the interferometer of the breadboard instrument. All the components of this instrument are commercially available. The light from the source was diffused at a small diameter iris and collimated by a spherical lens before entering the interferometer. The gratings are imaged on the detector array. All the measurements have been dark-field corrected. The two-dimensional CCD image was binned to form ten rows (interferograms) with 640 samples each. For the following discussion, we present the data from row 7.

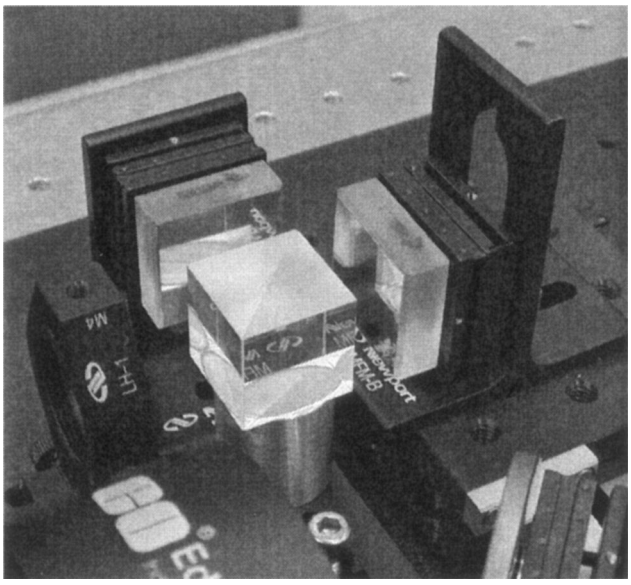

Fig. 2. Interferometer of the visible/near-infrared breadboard instrument. The input is on the lower left-hand side of the cubic beam splitter. The gratings are mounted using commercial three-point mounts. The grating on the right is mounted on a translation stage and can be moved away or toward the beam splitter. All the components of this breadboard spectrometer are commercially available (see also Table 1).

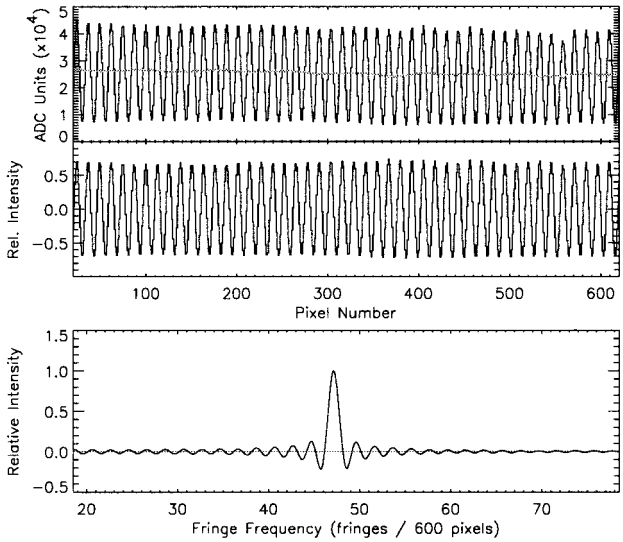

Fig. 3. Top panel: raw monochromatic interferogram (black) and the nonmodulated signal (gray) measured by blocking one interferometer arm at a time and adding the two measurements. Center panel: interferogram after application of the balanced arm flatfielding method. Bottom panel: real (black) and imaginary (gray) parts of the spectrum calculated from the corrected interferogram by phase correction, zero filling, and Fourier transformation. Since an unresolved line source was used for this measurement, the spectrum represents the instrumental line shape function.

B. Example for Balanced-Arm Flatfielding

The upper panel of Fig. 3 shows a raw, monochromatic interferogram (black) and the measured nonmodulated component (gray). The measurement of the nonmodulated component was obtained by blocking one interferometer arm at a time by using a piece of black paper and adding the two measurements. The nonmodulated part of the interferogram shows little pixel-to-pixel variation, indicating very similar pixel sensitivity. A slight decrease in the nonmodulated signal can be seen at approximately pixel 560, which is also visible as a signal decrease in the raw interferogram. The center panel of Fig. 3 shows the interferogram after the balanced arm flatfielding approach was applied. Since the pixel-to-pixel sensitivity variations are small in this example, the corrected interferogram looks similar to the raw interferogram. The flatfield correction improves the problem at approximately sample 560, but even after the correction a slight irregularity can be identified, which indicates that it is not caused by a difference in detector sensitivity. The bottom panel of Fig. 3 shows the real and imaginary parts of the spectrum that were retrieved by zero filling and Fourier transforming the interferogram. The remaining instrumental effect at approximately sample 560 is so small that the real part of the spectrum shows no significant deviation from a sinc function, which is expected from the finite length interferogram and an unresolved laser line source.

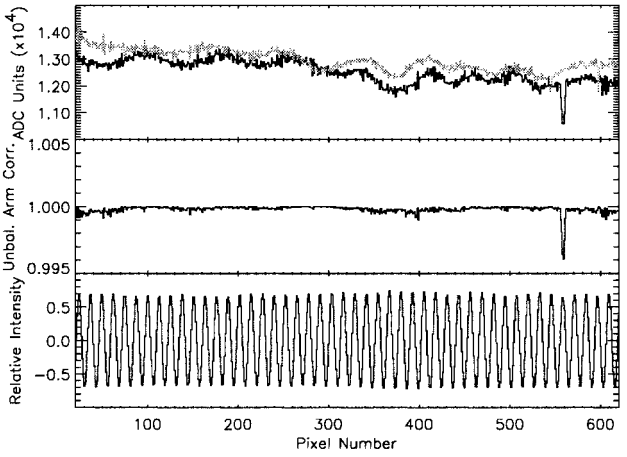

Fig. 4. Top panel: nonmodulated interferogram components measured with one arm blocked. Center panel: correction factor for the multiplicative term of the modulated interferometer part that is caused by the unbalanced arm contributions. Bottom panel: corrected interferogram.

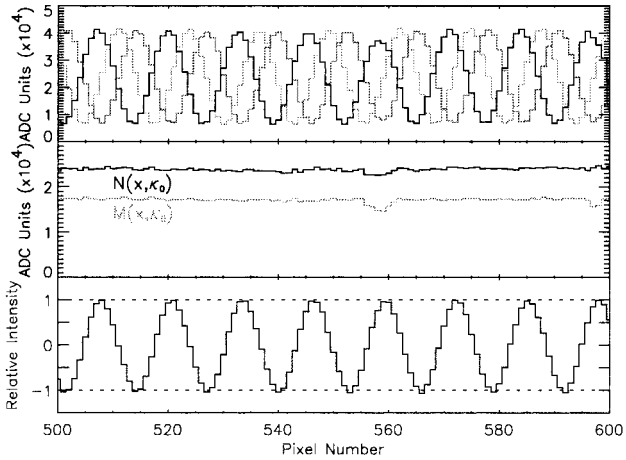

Fig. 5. Top panel: raw interferograms for three different grating locations resulting in a phase shift for each interferogram. Center panel: nonmodulated interferogram part (black) and the envelope of the modulated interferogram part (gray) as calculated from the raw interferograms. Bottom panel: corrected interferogram.

C. Example for Unbalanced-Arm Flatfielding

The upper panel of Fig. 4 shows the nonmodulated components of the spectrum for the two interferometer arms. They are measured by blocking one arm at a time. The contributions from both arms are not perfectly balanced for this interferometer. Some features are common to both arms, others are not. For example, the feature at pixel 560 is present only in one interferometer arm, indicating that it is a scratch, a manufacturing defect, or contamination on the corresponding grating.

The middle panel of Fig. 4 shows the term $\{2[I_A(x)I_B(x)]^{1/2}\}/[I_A(x) + I_B(x)]$ that is needed to correct for the effect of the unbalanced-arm contributions on the envelope of the modulated part of the interferogram [Eqs. (11) and (12)]. Except for the region at approximately pixel 560, this correction factor is always within 0.1% of unity for this example.

The lower panel of Fig. 4 shows the interferogram after application of the unbalanced arm flatfielding method.

D. Example for Phase-Shift Flatfielding

Figure 5 shows the measurements $I_1(x)$, $I_2(x)$, and $I_3(x)$ [Eq. (13)] around the area of the grating imperfection. The different phase shifts of the interferogram were achieved by moving one grating by using a micrometer driven translation stage. The middle panel shows the modulated and nonmodulated contributions to the interferogram as calculated using Eqs. (14) and (15). The lower panel shows the corrected interferogram. The improvement made by this flatfielding approach to the area at approximately pixel 560 can be seen clearly by comparing the raw interferograms in the upper panel to the corrected interferogram in the lower panel.

Figure 6 shows the nonmodulated and modulated components for the entire interferogram in the upper panel and the corrected interferogram in the center. The lower panel shows the retrieved spectrum and the difference between the corrected and the uncorrected spectrum multiplied by 10.

The example data we used to illustrate the flatfielding techniques are of high quality, i.e., the beam splitter, grating, exit optics, and detector elements did not cause major flatfield inhomogeneities. Depending on the wavelength region, such high quality components might not always be available. In these cases, a proper flatfield correction gains in importance.

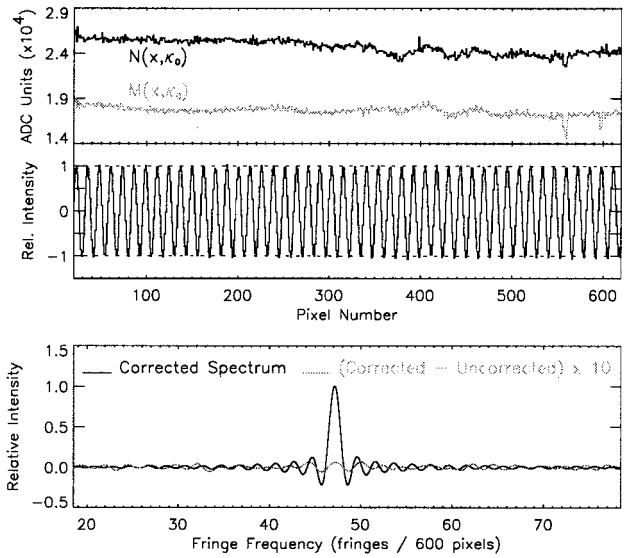

Fig. 6. Top panel: nonmodulated interferogram part (black) and the envelope of the modulated interferogram part (gray) as in the center panel of Fig. 5 but for the entire interferogram. Center panel: corrected interferogram. Bottom panel: real part of the corrected spectrum and the difference between the corrected and uncorrected spectrum multiplied by 10.

6. Conclusion

Variations in optics and detector pixels have long been recognized as a data analysis issue for all spectrometers that use detector arrays. We have presented three methods to correct for pixel-to-pixel variations in spatial heterodyne spectroscopy. When the flatfield error is dominated by the sensitivity variations in the detector array the balanced arm approach is appropriate. When significant differences in the signal from the two interferometer arms exist, the unbalanced arm approach is appropriate. When the gratings exhibit significant irregularities such as scratches, the phase-shift flatfielding approach is appropriate. All flatfielding corrections require additional measurements. The easiest way to obtain the necessary flatfield measurements for the first two methods is to block one interferometer arm at a time. The third method requires a change of the optical path length in one arm, which is usually harder to achieve, but is possible by moving the grating, pressure scanning one arm, or tilting a plane-parallel plate in one arm.

In principle, any interferogram measured by one particular spectrometer can be flatfield corrected using one set of flatfield measurements. However, care needs to be taken to eliminate effects that could change the flatfield such as thermal distortion of the instrument causing a shift or magnification change of the imaged interferogram. If the flatfield is likely to change with time, e.g., due to extreme thermal conditions, it may be necessary to record flatfield measurements periodically during the observation.

Funding for this research was provided by the Office of Naval Research. Additional support for the breadboard instrument was provided by the Naval Research Laboratory, Chemistry Division. The authors thank Joel G. Cardon (Space Dynamics Laboratory, Utah) and Fred L. Roesler (University of Wisconsin-Madison) for their assistance in building the breadboard, comments, and helpful discussions.

References

1. P. Cheben, I. Powell, S. Janz, and D. Xu, "Wavelength-dispersive device based on a Fourier-transform Michelson-type arrayed waveguide grating," Opt. Lett. **30,** 1824–1826 (2005).
2. J. M. Harlander, R. J. Reynolds, and F. L. Roesler, "Spatial heterodyne spectroscopy for the exploration of diffuse interstellar emission lines at far ultraviolet wavelengths," Astrophys. J. **396,** 730–740 (1992).
3. J. M. Harlander, H. T. Tran, F. L. Roesler, K. P. Jaehnig, S. M. Seo, W. T. Sanders, and R. J. Reynolds, "Field-widened spatial heterodyne spectroscopy: correcting for optical defects and new vacuum ultraviolet performance tests," in *EUV, X-Ray and Gamma-Ray Instrumentation of Astronomy V,* O. E. Siegmund and J. Vallerga, eds., Proc. SPIE **2280,** 310–319 (1994).
4. J. M. Harlander, F. L. Roesler, J. G. Cardon, C. R. Englert, and R. R. Conway, "SHIMMER: A spatial heterodyne spectrometer for remote sensing of Earth's middle Atmosphere," Appl. Opt. **41,** 1343–1352 (2002).
5. J. M. Harlander, "Spatial heterodyne spectroscopy: interferometric performance at any wavelength without scanning," Ph.D. dissertation (University of Wisconsin-Madison, 1991).
6. C. R. Englert, J. M. Harlander, J. G. Cardon, and F. L. Roesler, "Correction of phase distortion in spatial heterodyne spectroscopy," Appl. Opt. **43,** 6680–6687 (2004).
7. J. M. Harlander, F. L. Roesler, C. R. Englert, J. G. Cardon, R. R. Conway, C. M. Brown, and J. Wimperis. "Robust monolithic ultraviolet interferometer for the SHIMMER instrument on STPSat-1," Appl. Opt. **42,** 2829–2834 (2003).
8. C. R. Englert, J. T. Bays, J. C. Owrutsky, and J. M. Harlander, "SHIM-fire breadboard instrument design, integration and first measurements," NRL Memorandum Report NRL/MR/7640-05-8926 (Naval Research Laboratory, 2005).